

AGN feedback in the Phoenix cluster

C. Pinto,^{1*} C. J. Bambi,^{1,2} J. S. Sanders,³ A. C. Fabian,¹
 M. McDonald,⁴ H. R. Russell,¹ H. Liu,¹ and C. S. Reynolds,^{1,2}

¹*Institute of Astronomy, Madingley Road, CB3 0HA Cambridge, United Kingdom*

²*Department of Astronomy, University of Maryland, College Park, MD 20742-2421, USA*

³*Max-Planck-Institut für extraterrestrische Physik, Giessenbachstrasse 1, 85748 Garching, Germany*

⁴*Kavli Institute for Astrophysics and Space Research, MIT, 77 Massachusetts Avenue, Cambridge, MA 02139, USA*

Accepted 2018 August 8. Received 2018 August 3; in original form 2018 April 20

ABSTRACT

Active galactic nuclei (AGN) release a huge amount of energy into the intracluster medium (ICM) with the consequence of offsetting cooling and star formation (AGN feedback) in the centers of cool core clusters. The Phoenix cluster is among the most massive clusters of galaxies known in the Universe. It hosts a powerful starburst of several hundreds of Solar masses per year and a large amount of molecular gas in the center. In this work we use the high-resolution Reflection Grating Spectrometer (RGS) on board XMM-Newton to study the X-ray emitting cool gas in the Phoenix cluster and heating-cooling balance. We detect for the first time evidence of O VIII and Fe XXI–XXII emission lines, the latter demonstrating the presence of gas below 2 keV. We find a cooling rate of $350 \pm_{200}^{250} M_{\odot} \text{ yr}^{-1}$ below 2 keV (at the 90% confidence level), which is consistent with the star formation rate in this object. This cooling rate is high enough to produce the molecular gas found in the filaments via instabilities during the buoyant rising time. The line broadening indicates that the turbulence ($\sim 300 \text{ km s}^{-1}$ or less) is below the level required to produce and propagate the heat throughout the cool core. This provides a natural explanation for the coexistence of large amounts of cool gas, star formation and a powerful AGN in the core. The AGN activity may be either at a young stage or in a different feedback mode, due to a high accretion rate.

Key words: X-rays: galaxies: clusters – galaxies: active – turbulence.

1 INTRODUCTION

Clusters of galaxies are extraordinary laboratories where highly energetic astrophysical phenomena are in action. The study of the intracluster medium (ICM) embedded in their deep gravitational well allow us to understand the role of the strong energetic throughput from the active galactic nuclei (AGN) present in the individual galaxies into their surroundings over large scales up to a hundred kpc or more. A substantial fraction of galaxy clusters show a highly peaked density profile which implies that the central cooling time can be of an order of magnitude lower than the current age of the Universe (cool core clusters, e.g. Hudson et al. 2010). In the absence of heating, this would imply the cooling of hundreds of Solar masses of gas per year below 10^6 K (Fabian 1994) for the massive clusters, with a consequent star formation rate of a similar order of magnitude.

The best UV and X-ray indicators of cool gas are O VI emission lines (peaking at $T \sim 3 \times 10^5 \text{ K}$), O VII ($T \sim 2 \times$

10^6 K) and Fe XVII ($T \sim 6 \times 10^6 \text{ K}$). High-resolution UV and X-ray spectra of ICM were therefore expected to show bright lines, which instead turned out to be much weaker at levels of about $30 M_{\odot} \text{ yr}^{-1}$ or lower (see e.g. Bregman et al. 2005, 2006, Peterson et al. 2003 and Pinto et al. 2014).

There is a wealth of highly energetic phenomena occurring in the cores and in the outskirts of clusters of galaxies. Galactic mergers and gas sloshing within the gravitational potential may release large amounts of energy in the outskirts via shocks and turbulence injection (see e.g. Ascasi-bar & Markevitch 2006; Lau et al. 2009). However, there is a growing consensus that AGN are the most relevant sources of heating in cluster cores, particularly through their powerful relativistic jets (AGN kinetic / radio mode feedback, see e.g. Churazov et al. 2000 and Fabian 2012). For instance, the work done by AGN to inflate bubbles in the surrounding ICM gas proves to be equal if not stronger than the cooling rates McNamara & Nulsen (2007). There are several mechanisms through which the energy can be released into the ICM. Two elegant solutions involve dissipation of tur-

* E-mail: cpinto@ast.cam.ac.uk

bulence (see e.g. Zhuravleva et al. 2014) or sound waves (see e.g. Fabian et al. 2003, 2017).

There seems to be evidence that the extreme radio mode of AGN feedback has been operating in a steady way for the past 5 Gyr (see, e.g., Hlavacek-Larrondo et al. 2012 and McDonald et al. 2013), but this research field is still rather young and in development. Measurements of AGN-induced turbulence are therefore key to test whether some scenarios of AGN feedback and cooling-heating balance are feasible. This is crucial to understand if there is enough energy in the ICM to propagate the heat throughout the cool core.

It is possible to place constraints on turbulence by measuring the velocity broadening of the X-ray emission lines produced by the hot ICM. The Reflection Grating Spectrometers (RGS, den Herder et al. 2001) on board XMM-Newton are currently the only X-ray instruments which have enough collecting area and spectral resolution to enable this measurement. However, this is not very straightforward because the spectrometers do not possess an appropriate slit and therefore instrumental broadening has to be accounted for. Sanders et al. (2010) made the first measurement of cluster velocity broadening using the luminous cluster A 1835 at redshift 0.25. Due to the limited spatial extent of its bright core, instrumental broadening was minimal and an upper limit of 274 km s^{-1} was obtained. Sanders & Fabian (2011) constrained turbulent velocities for a large sample of 62 clusters, groups, and elliptical galaxies observed with XMM-Newton/RGS. Half of them show velocity broadening below 700 km s^{-1} . Recently, Sanders & Fabian (2013) used continuum-subtracted emission line surface brightness profiles to account for the spatial broadening. Pinto et al. (2015) focused on nearby objects using a catalog of 44 sources, the CHEERS sample, consisting of bright clusters, groups of galaxies, elliptical galaxies with a $\gtrsim 5\sigma$ detection of the O VII 1s–2p line at 19 \AA and with a well-represented variety of strong and weak cool-core objects. They confirmed the results obtained by Sanders & Fabian (2013) in more distant objects despite the more severe instrumental broadening due to the short distances ($z < 0.1$). Pinto et al. (2015) also showed that the upper limits on the Mach numbers are typically larger than the values required to balance cooling, suggesting that dissipation of turbulence may be high enough to heat the gas and to prevent cooling.

Turbulence in giant elliptical galaxies has also been constrained with an alternative method which uses the ratio of the Fe XVII emission lines detected in the RGS spectra (see, e.g., Werner et al. 2009, de Plaa et al. 2012, Pinto et al. 2016, Ogorzalek et al. 2017). When the velocity broadening is low, the gas is optically thick in the 15 \AA line due to resonant scattering, while the 17 \AA lines remain optically thin. Comparison between the observed line ratios with simulations for different Mach numbers constrains the level of turbulence. This method is very efficient for cool ($kT < 0.9 \text{ keV}$) giant elliptical galaxies rich in Fe XVII emission lines, but it is significantly limited by the systematic uncertainty ($\sim 20\%$) in the line ratio for an optically thin plasma. Currently, there are no facilities that allow the use of this technique on clusters of galaxies since the optical depth of the higher ionisation lines, typical of clusters, are smaller than those of the Fe XVII lines or they are out of the RGS energy band.

Another alternative method to constrain turbulence interprets the surface brightness fluctuations commonly seen

in X-ray atmospheres of clusters as turbulent fluctuations (see, e.g., Sanders & Fabian 2012, Zhuravleva et al. 2014, Walker et al. 2015 and Eckert et al. 2017). The measurements imply motions of one to a few hundred km s^{-1} .

As of today, and likely for the next years until the launch of missions like XRISM (a.k.a. XARM) and ATHENA (for a review see, e.g., Nandra et al. 2013 and Guainazzi & Tashiro 2019), the most accurate measurement of line broadening and, therefore, constraint on turbulence, has been obtained by the *Hitomi* observations of the Perseus cluster of galaxies (Hitomi Collaboration 2016). The soft X-ray microcalorimeter (SXS) onboard *Hitomi*, the first successfully operative in space, measured an average line broadening of $164 \pm 10 \text{ km s}^{-1}$ in a region between 30 and 60 kpc from the central AGN, thanks to an astonishing and unprecedented high spectral resolution of 4.9 eV in the Fe K energy band. Further work accounting for PSF effects showed that in several regions of the cluster core the turbulence could be lower than 100 km s^{-1} (Hitomi Collaboration 2017). These motions may not be able to propagate throughout the cluster rapidly enough to offset radiative losses at each radius of the cluster (Fabian et al. 2017).

In parallel work (Pinto et al. in prep) we have made a large catalog using all the XMM-Newton observations of clusters and groups of galaxies and ellipticals. The main goal is to constrain turbulence and other physical characteristics of a statistical sample of 150 galaxy clusters up to redshift 0.6 using high-resolution RGS spectra. This catalog includes and significantly extends what was previously done in Sanders & Fabian (2013) and Pinto et al. (2015). We also use a new technique to account for instrumental broadening that has been introduced in a very recent paper (Bambic et al. 2018). It was tested on three clusters at different redshifts with an observation quality among the best in our sample (A 1835, A 2204, and MACS J2229.7-2755). Upper limits of $200\text{--}250 \text{ km s}^{-1}$ were obtained on turbulence, confirming that it might be not high enough to propagate the heat throughout the cool core.

In this work we study the Phoenix cluster (SPT-CLJ2344-4243), the most distant object in our XMM-Newton/RGS catalog ($z = 0.596$), the most luminous X-ray cluster known and one of the most massive clusters ($\sim 2 \times 10^{15} M_{\odot}$, see Williamson et al. 2011 and McDonald et al. 2012). It also exhibits a starburst of $500\text{--}800 M_{\odot} \text{ yr}^{-1}$ (see, e.g., McDonald et al. 2015 and Mittal et al. 2017), which is among the largest found in the local Universe ($z < 1$). McDonald et al. (2015) found large amounts of mildly-ionized gas, such as He II, O III and O VI, which is not consistent with cooling but rather suggests that an ionized wind is driven by the AGN and/or the starburst. ALMA observations of the CO(3-2) line emission have shown a huge amount of molecular gas around $2 \times 10^{10} M_{\odot}$ (Russell et al. 2017). The molecular gas might have been uplifted directly by the radio bubbles or formed via instabilities in low entropy gas lifted by the jet. Tozzi et al. (2015) observed the Phoenix cluster for 250 ks with XMM-Newton and found a cooling rate between $100\text{--}1000 M_{\odot} \text{ yr}^{-1}$ with the large uncertainties mainly driven by the calibration between the CCD cameras on board the satellite combined with their low spectral resolution. They also used the RGS gratings and claimed to have not found any lines from ionization states below

Table 1. XMM-Newton and Chandra log of observations.

OBS_ID (XMM)	$t_{\text{RGS}}^{(a)}$ (ks)	$c_{\text{RGS}}^{(c)}$ (counts)	$t_{\text{MOS}}^{(b)}$ (ks)	OBS_ID <i>Chandra</i>	$t_{\text{ACIS}}^{(d)}$ (ks)
0693661801	16.5	1.8k	16.1	13401	11.9
0722700101	130.6	14.1k	128.0	16135	57.3
0722700201	93.0	10.1k	92.0	16545	59.1

^(a) RGS1, RGS2 and ^(b) MOS1 net exposure time.

^(c) RGS total counts and ^(d) ACIS-I net exposure time.

Fe XXIII with an upper limit on the cooling rate of about $500 M_{\odot} \text{ yr}^{-1}$ below 3 keV.

The presence of a high star formation, a high cooling rate and a powerful AGN in the Phoenix cluster casts doubts on the efficiency of AGN feedback to balance cooling. Therefore, we perform an in-depth study of the XMM-Newton observations of the Phoenix cluster with particular focus on the high-resolution spectrometers in order to obtain more accurate measurements of the cooling rate and the turbulent broadening. We find that $350 \pm_{120}^{150}$ (68%) \pm_{200}^{250} (90%) $M_{\odot} \text{ yr}^{-1}$ are cooling below 2 keV in the cluster core and that the turbulence level is likely not adequate to fully propagate AGN heating throughout the cool core. The cooling rate is instead high enough to produce the large amount of molecular gas found in the form of filaments if we assume that the gas cools during the bubble rising time.

We present the data in Sect. 2 and the spectral modeling in Sect. 3. We discuss the results in Sect. 4 and give our conclusions in Sect. 5.

2 THE DATA

The observations used in this paper are listed in Table 1. The XMM-Newton satellite is provided with two main X-ray instruments: RGS (Reflection Grating Spectrometer) and EPIC (European Photon Imaging Camera). We use RGS for the spectral analysis and EPIC (MOS1 detector, which is aligned with RGS) for imaging. The EPIC/MOS1 surface brightness profiles are necessary to account for line instrumental broadening due to the slitless nature of the RGS spectrometers. This is done following the procedures used in Pinto et al. (2015) with important updates shown in Bambi et al. (2018).

We perform the data reduction with the XMM-Newton Science Analysis System (sas) v16, CalDB as of January 2018. We process the RGS data with the SAS task *rgsproc* and the MOS1 data with *emproc* to produce event files, spectra, and response matrices for RGS (both 1 and 2) and images for MOS1. Following the standard procedures, we filter the MOS event list for bad pixels, bad columns, cosmic-ray events outside the field of view (FOV), photons in the gaps (FLAG = 0), and apply standard grade selection, corresponding to PATTERN ≤ 12 .

We correct for contamination from soft-proton flares through the SAS task *evselect* by extracting light curves for MOS1 in the 10–12 keV energy band, while we use the data from the CCD number 9 for RGS, where hardly any emission from the source is expected. The light curves are grouped in 100 s intervals and all the time bins with a count rate above 0.35 c/s and 0.15 c/s are rejected for MOS and

RGS, respectively. We build the good time interval (GTI) files with the accepted time events for the MOS and RGS data through the SAS task *tabgtigen* and reprocess the data again with *rgsproc* and *emproc*. For RGS 1 and 2 we join the GTI and obtain the same exposure times. The RGS 1-2 and MOS 1 total clean exposure times are quoted in Table 1.

2.1 RGS spectra

The RGS 1 and 2 spectra are extracted using as centroid $(\alpha, \delta) = (23 : 44 : 43.9, -42 : 43 : 13.7)$ and a width of 50 arcsec by adopting the mask *xpsfincl* = 90 in the *rgsproc* ($\sim \pm 170$ kpc for a standard Λ CDM cosmology with $H_0 = 70 \text{ km s}^{-1} \text{ Mpc}^{-1}$, $\Omega_M = 0.27$ and $\Omega_{\Lambda} = 0.73$). In order to subtract the background we test both the standard background spectrum which is extracted beyond the 98% of the RGS point spread function (PSF, *xpsfexcl* = 98 in the *rgsproc*) and the model background spectrum, which is a template background file based on the count rate in CCD 9. Normally one would use the model background for an extended source, but due to the large distance we can safely use the observation background since it is extracted beyond $\pm 1.4'$. The background spectra are indeed comparable, provide consistent results and about 26,000 net source counts in the RGS 6–33 Å wavelength band. More detail on the background is provided in Appendix A.

The spectra are converted to the SPEX¹ format through the SPEX task *trafo*. During the spectral conversion, we choose the option of *sectors* in the task *trafo* to create as many sectors as there are different exposures. This permits us to simultaneously fit the multiple RGS spectra by choosing which parameters to either couple or unbind in the spectral models of different observations. We focus on the first-order spectra because the second-order spectra have too poor statistics. We also combine source and background spectra, and responses from all observations and from both RGS instruments using the SAS task *rgscombine* for plotting purposes only. The stacked spectrum is shown in Fig. 1 labelling the rest-frame wavelengths of the strongest emission lines commonly found in deep RGS spectra of clusters and groups of galaxies.

2.2 MOS images

We produce MOS1 images in the 6 – 35 Å wavelength band (see Fig. 2), which is the same range used for the RGS spectroscopy, and extract surface brightness profiles to model the RGS line spatial broadening with the standard dispersion equation:

$$\Delta\lambda = 0.138 \Delta\theta \text{ \AA} / m, \quad (1)$$

where $\Delta\lambda$ is the wavelength broadening, $\Delta\theta$ is the source extent in arcseconds and m is the spectral order (see the XMM-Newton Users Handbook). The surface brightness is extracted using a region of $50''$ width and a length of $10''$ with the SPEX task *rgsvprof* (see, e.g., Pinto et al. 2015). The RGS instrumental line broadening as measured through the MOS1 surface brightness profile of the Phoenix cluster is shown in Fig. 3 (black solid line).

¹ www.sron.nl/spex

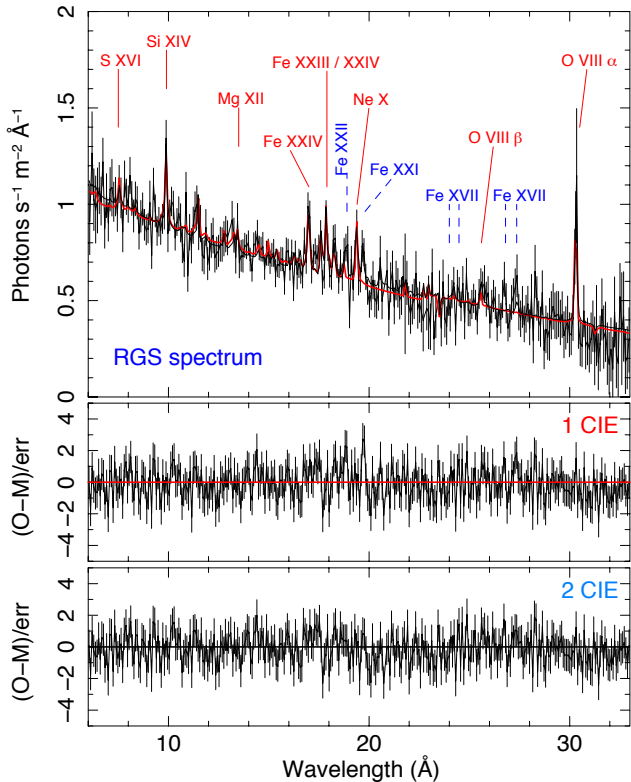


Figure 1. RGS spectrum of the Phoenix cluster with overlaid isothermal model of gas in collisional equilibrium (red) and a two-temperature model (black). Emission lines commonly detected in RGS spectra of cool core clusters are labelled at the observed wavelengths with the blue dashed ones referring to lines from cool gas. Bottom plots show the residuals to each model. Note how the second component improves the fit near the Fe XVII and Fe XXI-XXII main transitions.

Table 2. XMM-Newton/RGS best-fit isothermal *cie* model.

$n_e n_H V$	kT	$v_{\text{mic}}(2D)$	$C/d.o.f.$	O/H
4.52 ± 0.06	7.0 ± 0.5	230 ± 220	1105/951	0.38 ± 0.12
Ne/H	Mg/H	Si/H	S/H	Fe/H
0.43 ± 0.12	0.45 ± 0.25	0.75 ± 0.16	0.5 ± 0.3	0.8 ± 0.2

Abundances are in proto-Solar units (Lodders & Palme 2009), emission measure $n_e n_H V$ in 10^{74}m^{-3} , temperature in keV and micro-turbulence 2D velocity in km s^{-1} as default in SPEX.

We also fit the broadening profile with 3 different models using QDP/PLT²: a single Gaussian, two Gaussian and three Gaussian lines. The single Gaussian line and the narrowest Gaussian of the multi component models are also shown in Fig. 3, but renormalized for plotting purposes.

3 SPECTRAL ANALYSIS

3.1 Isothermal collisional equilibrium model

Our analysis focuses on the 6 – 35 Å first order RGS spectra, where the source counts are above the background and

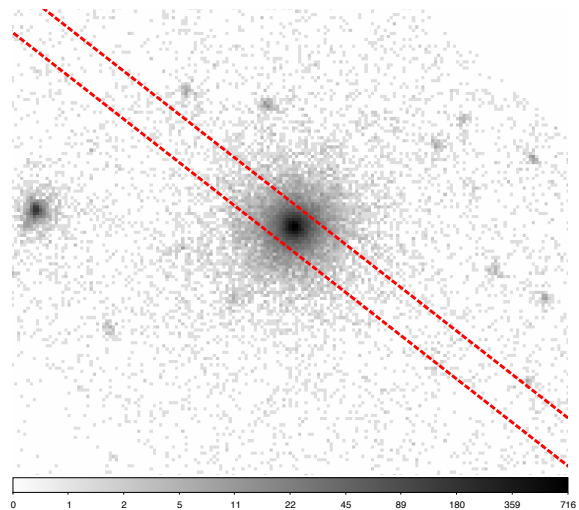


Figure 2. EPIC/MOS 1 image of the Phoenix cluster with the RGS extraction region of width of 50 arcsec.

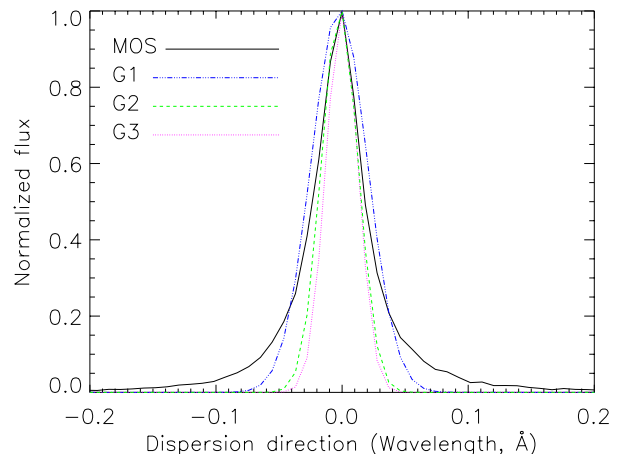


Figure 3. RGS line spatial broadening as computed through the MOS 1 surface brightness profile and Eq. 1. The lines show the narrowest Gaussian obtained by fitting three different models with either one or two or three Gaussian lines.

cover the 4–22 Å rest-frame wavelength range. This includes K shell emission lines of sulphur, silicon, magnesium, neon, oxygen and the L shell lines of iron and nickel. We perform the spectral analysis with SPEX version 3.04.00. We scale the elemental abundances to the proto-Solar abundances of Lodders & Palme (2009), which are the default in SPEX, use C-statistics and adopt 1σ errors, unless otherwise stated.

We describe the ICM emission with an isothermal plasma model of collisional ionization equilibrium (*cie*). The basis for this model is given by the MEKAL code, but several updates have been included (see the SPEX manual). Free parameters in the fits are the emission measure $Y = n_e n_H V$, the temperature T , the micro-turbulence 2D velocity broadening and the abundances (O, Ne, Mg, Si, S and Fe). The abundances of all the other elements are coupled to iron. The *cie* emission model is corrected for redshift (0.596) and Galactic absorption ($N_H = 1.7 \times 10^{24} \text{m}^{-2}$, Kalberla et al. 2005) through the *hot* model with very low temperature (0.5

² <https://wwwastro.msfc.nasa.gov/qdp/>

eV). This component accounts for both absorption edges and lines of neutral and low-ionisation species in the ISM (see, e.g., Pinto et al. 2013).

We do not explicitly model the cosmic X-ray background in the RGS spectra because any diffuse emission feature would be smeared out into a broad continuum-like component. The Phoenix cluster is known to host a powerful highly-obscured AGN; its emission is negligible in the soft (< 2 keV) X-ray band (see Tozzi et al. 2015 and references therein) and we therefore do not include it in our model. For each exposure, we simultaneously fit the RGS 1 and 2 spectra by adopting the same model, apart from the emission measures of the *cie* components which are uncoupled to account for the slightly different roll angles of the observations.

This simple plasma model provides a reasonably good fit of the RGS spectra as shown by Tozzi et al. (2015). Most strong lines are well described by the isothermal model, see Fig. 1 and Table 2. However, there are some emission-like features missed just near the rest-frame wavelengths of the strongest transitions of Fe xxI and xxII. It is therefore an interesting and useful exercise to formally search for indicators of cool gas before calculating any cooling rates. One may in principle just add a few Gaussian lines corresponding to the strongest transitions expected from gas cooler than that contributing to the strong Fe xxIII-xxIV lines.

3.2 Search for cool gas

In order to search for any weak lines produced by cool gas and therefore missed by our isothermal 7 keV model we prefer to perform a line scan over the RGS spectrum. Following the procedure used in Pinto et al. (2016), we search for any line emission on top of the continuum by fitting a Gaussian scanning over the 6 – 33 Å wavelength range with increments of 0.05 Å and calculating the ΔC -statistics. We adopt a linewidth (FWHM) of 160 km s⁻¹, which is the measurement obtained from *Hitomi* on Perseus (Hitomi Collaboration 2016). We repeat the procedure adopting linewidths ranging between 100 and 1000 km s⁻¹ without finding major effects on the line detection. Whilst running the scan we also turn off the line emission from the isothermal gas in order to check that the lines detected with highest significance indeed correspond to the strongest lines described by the isothermal model. The continuum model is basically bremsstrahlung emission. This is achieved with the `SPEX` command “*ions ignore all*”. We show the results of the RGS line scan in Fig. 4. Both the ΔC -statistics (ΔC) and the ratio between the normalization and its uncertainty of the Gaussian are plotted. The ΔC are multiplied by the sign of the Gaussian normalization to distinguish between emission and absorption-like features. No absorption line is found at ΔC of 9 or above corresponding to a normalization/error ratio of 3 or above.

It is straightforward to identify some isolated emission features with the strongest transitions in this energy band such as Fe xxIV (10.63 Å), Si xIV (6.19 Å), Ne x (12.135 Å) and O viII (18.97 Å). The O viII $K\alpha$ line is so strong that pops up within a spectral range that is already affected by the background and it was not shown in previous work on Phoenix. Two other interesting lines are also detected in correspondence of the strongest transitions to the ground

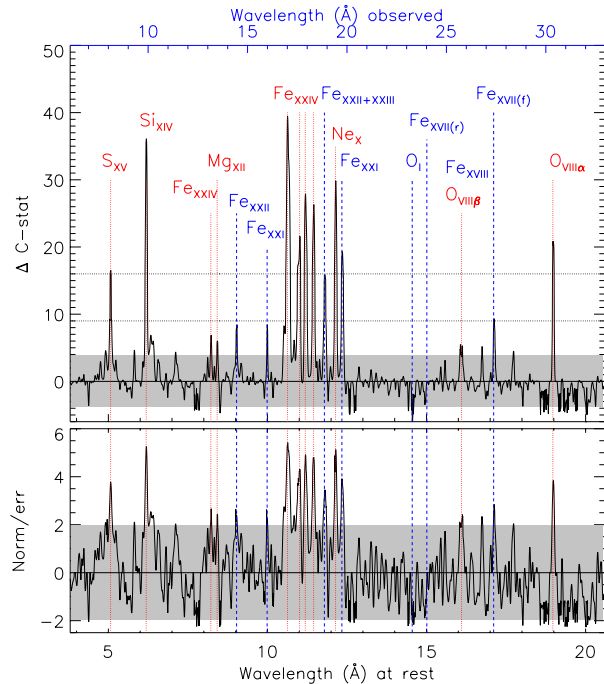


Figure 4. RGS Gaussian line search. The top panel shows the ΔC -stat multiplied by the sign of the line in order to distinguish both the significance and the type (emission/absorption-like) of each feature. The bottom panel shows the ratio between the normalization of the Gaussian and its error. The top and bottom X-axes show the observed and the rest-frame ($z=0.596$) wavelength range, respectively. The vertical dotted lines indicate the rest-frame transitions of the strongest emission lines, whilst the blue dashed ones refer to lines from cool gas. Shaded grey regions refer to features below the 2σ detection limit and the noise level.

state of Fe xxII-xxIII and xxI at (11.79 Å) and (12.34 Å), respectively, which indicates that there may be some gas well below 3 keV. Additional, fainter, features consistent with weaker Fe xxI-xxII transitions are found within 9–10 Å. We do not find strong lines from very cool gas such as Fe xvII, although there is a spike just at 17.1 Å where the forbidden line is expected. It is surprising that no Fe xvII resonant line is detected at 15.0 Å, but we notice that it falls near the absorption edge of the neutral oxygen in the Galactic ISM and where RGS 2 chip is missing, yielding half the effective area. Briefly, the RGS 2 detector misses the 20–24 Å observed wavelength range, while RGS 1 lost the 10.5–13.5 Å range. Luckily, RGS 1 and 2 complement each other, but the effective area in the shared bands (below 10.5 Å, 13.5–20 Å and above 24 Å in the observed frame) is boosted and increases the detectability of some spectral features. Another possibility would be that the 15.0 Å line is highly suppressed by resonant scattering as suggested for the Perseus cluster in Pinto et al. (2016).

3.3 Line significance

The statistical improvement to the best fit of the continuum model yielded by each line provides a crude estimate of the corresponding line significance. The lines detected are exactly those expected for a 7 keV cool core of a massive

Table 3. RGS line significance.

Ion	Fe XXIV	Fe XXII-XXIII	Fe XXI	Fe XVII(f)
λ (Å)	10.63±0.01	11.79±0.02	12.34±0.02	17.1±0.02
ΔC	40.20	15.70	19.75	9.54
% _{MAX}	99.99	99.99	99.99	99.80
% _{MCLE}	99.99	99.32	99.95	95.11
Ion	S XV	Si XIV	Ne X	O VIII
λ (Å)	5.06±0.01	6.19±0.01	12.14±0.01	18.97±0.02
ΔC	15.28	35.16	32.3	20.16
% _{MAX}	99.99	99.99	99.99	99.99
% _{MCLE}	99.46	99.99	99.99	99.95

Notes – Some of the strongest lines detected for each ion. Fe XXII-XXIII lines at 11.7–11.8 Å cannot be resolved. Wavelengths account for a redshift of 0.596. ΔC is the fit improvement of each line. %_{MAX} is the maximum confidence level calculated from the ΔC ; %_{MCLE} is the confidence level estimated with 10,000 Monte Carlo simulations to account for the look-elsewhere effect.

($M \sim 2 \times 10^{15} M_{\odot}$) cluster like Phoenix and are detected at their rest wavelengths.

In Table 3 we quote the wavelengths and the statistical improvements of the strongest lines detected as expected from their dominant transitions. The Fe XXII-XXIII lines merge into one feature that is closer to the Fe XXI line centroid. The confidence levels (CL) corresponding to the measured ΔC values are also reported as %_{MAX} and reported as to 99.99 whenever they match or surpass this threshold.

In order to estimate a rigorous and more conservative line significance we need to correct for any fake detection and account for the “look-elsewhere” effect. This is done with Monte Carlo simulations. We use the bremsstrahlung continuum as a template model to simulate 10,000 spectra with the same response matrix, exposure time and background as the actual RGS data. Then an identical line search is performed as for the original data. The significance of a line found in the data is computed as the ratio of the number of simulations that do not show a line with the same or higher ΔC value to all performed simulations. The results of the simulations are also shown in Table 3 (%_{MCLE}). Regardless of the method, several lines are detected well above 3σ . However, we notice that our lines are not random species detected at random locations. Fe XXI-XXII, for instance, are the strongest transitions expected after the well-known Fe XXIII-IV lines and are at their expected wavelengths. For this reason the Monte Carlo result has to be regarded as a very pessimistic case. We examine the Fe XXII-XXIII confusion by including all the lines of the best-fit baseline model and check the fluxes predicted by the latest AtomDB and SPEX databases. The improvement obtained by adding a further Fe XXII line is ΔC -stat = 13 (compared to the total of 15.7), which for a single line detection is still significant albeit at lower levels, with Fe XXII providing the strongest contribution at 11.79 Å. The transitions are the strongest expected from AtomDB and SPEX: Fe XXI $1s^2 2s^2 2p^1 3d^1 \rightarrow 1s^2 2s^2 2p^2$ (Level 40 \rightarrow 1) and Fe XXII $1s^2 2s^2 3d^1 \rightarrow 1s^2 2s^2 2p^1$ (Level 21 \rightarrow 1).

3.4 Cooling rate

In order to place constraints on the amount of gas cooling from 7 keV all the way down to 0.1 keV we refit the RGS

spectrum adding a cooling flow model to the isothermal gas reported in Table 2. The *cf* model in SPEX calculates the spectrum of a standard isobaric cooling flow. The differential emission measure distribution for the isobaric cooling flow model can be written as

$$D(T) \equiv \frac{dY(T)}{dT} = \frac{5\dot{M}k}{2\mu m_{\text{H}}\Lambda(T)} \quad (2)$$

where \dot{M} is the mass deposition rate, k is Boltzmann’s constant, μ the mean molecular weight (0.618 for a plasma with a 0.5 Solar metallicity), m_{H} is the mass of a hydrogen atom, and $\Lambda(T)$ is the cooling function. The cooling function is calculated by SPEX for a grid of temperatures and for 0.5 Solar metallicity. The spectrum is evaluated by integrating the above differential emission measure distribution between a lower and an upper temperature boundary.

At first we use a complex model with five *cf* components plus the isothermal *cie* all corrected by redshift and absorption. The aim is to understand how much gas is cooling between several temperature ranges (0.1–0.5, 0.5–1.0, 1.0–2.0, 2.0–3.0, 3.0–7.0 keV). The only free parameter in each *cf* is the cooling rate, \dot{M} , whilst the abundances are coupled to those of the *cie* component, which are constrained by the strongest lines. Obviously, there is a high degeneracy in the measurements due to low statistics owing to the large distance of the Phoenix cluster. We can only measure upper-limits on the amount of gas cooling within each temperature interval (see Fig. 5). Despite the degeneracy, a significant drop of gas cooling below 2 keV might be present.

In order to place tighter constraints and not to boost the degeneracy, we simplify the model by using only two cooling flow components (0.1–2.0, 2.0–7.0 keV) in addition of the isothermal gas model. We estimate that $350 \pm_{120}^{150}$ (68%) \pm_{200}^{250} (90%) $M_{\odot} \text{ yr}^{-1}$ are cooling below 2 keV. Obviously, this simple model broadly agrees with the more complex five *cf* components (see Fig. 5).

We also refit the RGS spectrum with a simple two-temperature model consisting of the baseline *cie* model plus an additional *cie* component. This additional cool component improves the fit by $\Delta C = 20.5$ for two additional degrees of freedom ($n_e n_{\text{H}} V_2 = 8.5 \pm 2.5 \times 10^{72} \text{ m}^{-3}$) and $kT_2 = 1.20 \pm 0.13$ keV, mainly constrained by the Fe XXI-XXII lines). Excluding these lines the fit improvement would be much smaller ($\Delta C = 7.5$) with $T \sim 1.1$ keV.

3.5 Instrumental broadening

The spectral fits yield a maximum line width corresponding to a velocity broadening $v_{\text{mic}}(1D) < 420 \text{ km s}^{-1}$ (90% upper limit or $\Delta C = 2.71$). This measurement, however, does not account for the fact that some of the broadening is due to the nature of the RGS detectors. The instrumental broadening can be subtracted using the surface brightness computed with the CCD detectors. This is achieved through the use of the *lpro* model in SPEX. The *lpro* receives as input the spatial broadening measured with the MOS 1 surface brightness profile and convolves it with the baseline spectral model:

$$\text{Spectrum} = (\text{hot} \times \text{redshift} \times \text{cie}) \otimes \text{lpro}.$$

The *lpro* component now accounts for the spatial broadening and the v_{mic} parameter of the *cie* component accounts for any leftover line broadening due to turbulence. A new fit

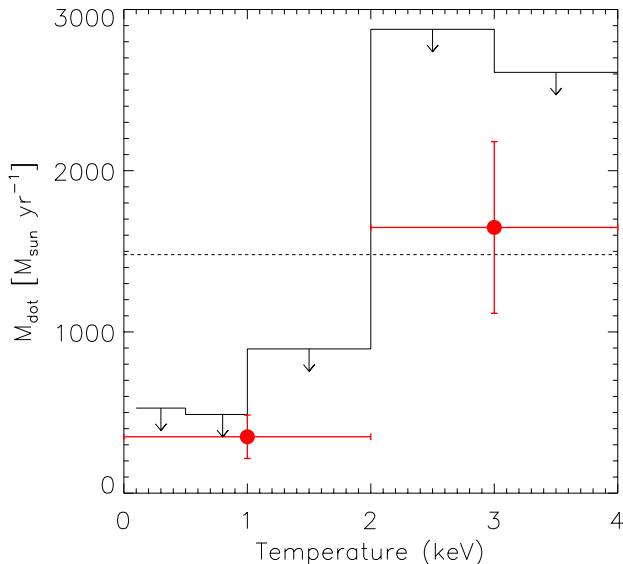


Figure 5. Constraints on cooling rates using two classical radiative cooling flow models (red points) and upper limits (black arrows) for a five-component cooling model on top of the isothermal CIE model.

of the RGS spectra with this model place the 90% upper limit of the velocity broadening down to 280 km s^{-1} .

Sanders & Fabian (2013) have shown that the CCD spatial profile is highly affected by the large scale distribution of the hot gas which mostly contributes to bremsstrahlung continuum rather than lines. The physical scale of the hot gas is much larger than that of the cool core that produces the emission lines detected in the RGS spectra (see, e.g., Pinto et al. 2016 for more detail on the link between the line widths and the location of the cool gas). This means that using the full spatial profile might result into an over-subtraction of the spatial broadening and, therefore, an under-estimate of the upper limit on the turbulence. Sanders & Fabian (2013) attempted at subtracting spatial profiles extracted in energy bands that include only strong lines. They obtained typical levels of $300\text{--}400 \text{ km s}^{-1}$ with systematic uncertainties of about 150 km s^{-1} .

In Bambic et al. (2018) we introduced a new method which consists of fitting three Gaussian lines to the spatial profile. The central Gaussian can be interpreted as the coldest core of gas, the outer Gaussian reproduces the bremsstrahlung continuum from hot hydrogen gas beyond the cluster core. The intermediate Gaussian models any smooth transition between cool and hot regions. This may prove to be necessary for highly multi-phase and nearby clusters such as Centaurus, but not crucial for an object like Phoenix. The narrowest Gaussian obtained by fitting a single Gaussian, two Gaussian and three Gaussian lines to the MOS spatial profiles are shown in Fig. 3. We test each of these three profiles independently as input of the *lpro* model as shown above. We obtain $v_{\text{mic}}(1D)$ 90% upper limits of about 400, 370 and 330 km s^{-1} using the narrowest of one, two and three Gaussian lines, respectively.

We also extract a spectrum in a smaller region (70% of the PSF, i.e. 100 kpc) and, interestingly, find that the line width strongly decreases with a 2σ (90%) upper limit of only

290 km s^{-1} (without any spatial broadening subtraction). This further supports our results obtained with the 90% PSF through the modelling of the spatial broadening.

Finally, we extract *Chandra* ACIS surface brightness profiles from the longest exposures along the RGS dispersion direction and produce spatial broadening profiles similarly to EPIC/MOS 1. We then fit models with 1, 2 and 3 Gaussians to measure the core spatial broadening. We find that the limits obtained using the *Chandra* data are systematically larger than those obtained with MOS data, but by only a small amount ($10\text{--}15 \text{ km s}^{-1}$).

3.6 Turbulence required for heat transfer

In Bambic et al. (2018) we showed that the balance between cooling and heating at any radius r within the cool core requires a minimum level of turbulence. This is in order to propagate the energy from the central AGN to that location. This translates into the following threshold:

$$\sigma_{1D(\text{km/s})} = 4.69 \times \left(\frac{r_{\text{kpc}} L_{44}}{M_{15}} \right)^{1/3} \quad (3)$$

where $L_{\text{cool}} = L_{44} \times 10^{44} \text{ ergs/s}$, $M_{\text{gas}} = M_{15} \times 10^{15} M_{\odot}$, $r = r_{\text{kpc}} \times 3.09 \times 10^{21} \text{ cm}$. In Bambic et al. (2018) we noticed that this approach provides conservative limits for the required propagation velocity of turbulence.

We use *MBProj2* (Sanders et al. 2018) to produce profiles for L_{44} and M_{15} from *Chandra* observations. The gas mass is estimated from the observed surface brightness with the assumptions of spherical symmetry and hydrostatic equilibrium. The profiles are computed assuming an NFW dark matter mass profile, using the same data, analysis procedure and BIN-NFW model as described in Sanders et al. (2018). The 68% statistical uncertainties on the turbulent velocity are computed from Monte Carlo fits of Eq. 3 to the velocity profiles, implementing error chains on each of the measured quantities. The error bars on the turbulent velocity calculated at each radius are shown in Fig. 6 and are compared with upper limits on turbulence as measured with the linewidths in the RGS spectra. It is clear that regardless of how severe is the subtraction of the instrumental broadening, the best constrained 90% upper limits on $v_{\text{mic}}(1D)$ lie below the velocity required to transfer heat throughout the cool core and offset radiative cooling, particularly within the inner 100 kpc. The use of a narrower extraction region and the spatial broadening profiles computed with *Chandra* supports these results.

4 DISCUSSION

4.1 Cooling and star formation rates

In this work we study the Phoenix cluster (SPT-CLJ2344-4243) in order to understand why such a massive cluster exhibits a strong starburst of $500\text{--}800 M_{\odot} \text{ yr}^{-1}$ in combination with a powerful AGN and a very low central cooling time (see, e.g., McDonald et al. 2012). This object is of high interest as it is also the most luminous X-ray cluster known and the most distant object in our XMM-*Newton*/RGS legacy catalog (Pinto et al. in prep). Phoenix is currently the only

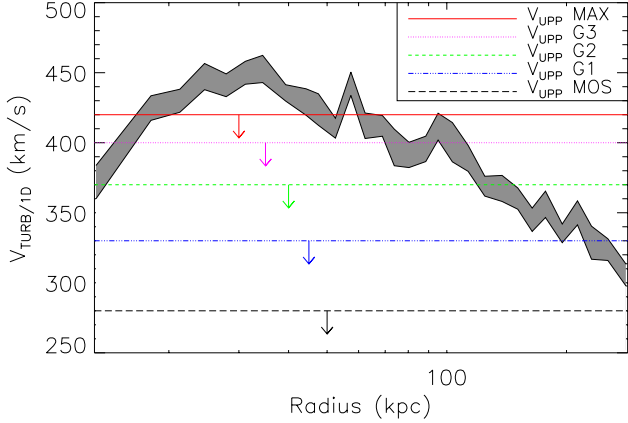


Figure 6. Constraints on turbulence. The grey region shows the turbulence required to propagate the heat throughout the cluster from the central AGN up to 250 kpc. The lines show the 90% upper limits obtained with the RGS spectral fits: total line width (top dotted line) compared to leftover broadening after subtracting the narrow Gaussian fits (dashed/dotted-dashed lines) or the full spatial MOS profile (bottom dashed line).

cluster at redshift 0.6 for which high-resolution X-ray spectroscopy is feasible. This technique is crucial in order to obtain reliable constraints on turbulence, abundances and emission measures of cool gas phases. Phoenix can also be regarded as an early stage and proxy for nearby, massive, cool core clusters.

We find that the amount of cool gas below 2 keV is consistent with a cooling rate of $350 \pm_{120}^{150}$ (68%) \pm_{200}^{250} (90%) $M_{\odot} \text{ yr}^{-1}$ (see Fig. 5), which agrees with the upper limits obtained by [Tozzi et al. \(2015\)](#). We detect for the first time evidence of O VIII and Fe XXI-XXII emission lines in the Phoenix cluster. These iron lines demonstrate the presence of gas below 2 keV. Our measured cooling rate is broadly consistent with the starburst rate, suggesting a possible link between the gas cooling in the inner core (< 100 kpc) and that involved in the starburst. Interestingly, the spectrum extracted in a narrower region (70% of the PSF, see Sect. 3.5) shows that the overall flux of the hot component decreases by 13%, while the cold component is consistent with being constant. This suggests that the cold gas is located in the innermost regions.

The tentative detection of Fe XVII forbidden and intercombination lines and the absence of the corresponding resonant line would suggest that this cool phase might be subject to some form of heating. This would agree with the detection of strong O VI in HST/COS spectra of the Phoenix cluster ([McDonald et al. 2015](#)). Unfortunately, the O VII lines are hidden within the noise and the high instrumental background around 35 Å; here the spectrum does not provide reliable constraints. However, we successfully model the Fe XVII emission lines and other cool gas features with a photoionized gas model. This is done by adding into our SPEX best-fit model an additional emission component through the PHOTEMIS code³ adopting a low ionization parameter of about $1 \text{ erg s}^{-1} \text{ cm}$. Our model predicts a total O VI luminosity of $10^{43} \text{ erg s}^{-1}$ or above, in agreement with the accurate

measurements obtained in the FUV with HST/COS spectra ([McDonald et al. 2015](#)).

The picture might be slightly more complicated since the molecular and neutral gas in the filaments could absorb some of the soft X-ray emission. This means that the cooling rate that we measure is possibly a lower limit. Unfortunately, without knowing the covering fraction and solid angle of this coolest phase as well as its location with respect to the soft X-ray emitting gas, it is difficult to estimate its column density and thus the unabsorbed soft X-ray emission.

4.2 Cooling versus heating propagation

The presence of both high star formation and cooling rates in the Phoenix cluster casts doubts on the efficiency of AGN feedback to balance cooling in this system. However, the AGN is certainly affecting the cluster and this can be seen, for instance, in the ALMA observations of the CO(3-2) line emission which show that approximately half of the molecular gas, $\sim 1 \times 10^{10} M_{\odot}$, is located mainly at the peripheries of the radio bubbles ([Russell et al. 2017](#)).

It is interesting to note that our cooling rate of $350 \pm_{120}^{150}$ (68%) \pm_{200}^{250} (90%) $M_{\odot} \text{ yr}^{-1}$ is high enough to produce the $160 \pm 50 M_{\odot} \text{ yr}^{-1}$ necessary to cool down into the molecules that are found in the filaments ($1 \times 10^{10} M_{\odot}$), assuming a buoyant rise time of 50–120 Myr for the bubbles (e.g., [Russell et al. 2014](#), [McNamara et al. 2014](#), [Russell et al. 2017](#)). Moreover, if we decouple the redshifts of the two thermal components in our RGS two component spectral fits (see bottom of Sect. 3.4), we find that the cool gas (1.2 keV, Fe XXI-XXII) has a systematic velocity of $+1000 \pm 400 \text{ km s}^{-1}$ on top of the redshift of the main 7 keV component. Despite the large uncertainties, this result resembles the velocity shift of 250 km s^{-1} found in the molecular gas, suggesting that these two phases may actually be related and that they are falling back towards the nucleus of the brightest cluster galaxy (BCG).

In order to place tight constraints on turbulence and estimate whether the energy stored in turbulent motions is high enough to balance radiative cooling, we perform an accurate high-resolution spectroscopic analysis. The total line width of the emission lines detected in the RGS spectrum is below 420 km s^{-1} (90% upper limit of the 1D micro-turbulence velocity). Using a newly introduced technique which accounts for instrumental broadening ([Bambic et al. 2018](#)), we show that the turbulence level in the Phoenix cluster is likely well below 400 km s^{-1} . Spectra extracted in narrower regions yield even lower limits (290 km s^{-1} , see Sect. 3.5). This result suggests similar values of turbulence detected in the Perseus cluster with *Hitomi* on similar physical scales ([Hitomi Collaboration 2016](#)), in the core of nearby giant elliptical galaxies through resonant scattering techniques ([Ogorzalek et al. 2017](#)) and several nearby clusters ([Sanders & Fabian 2013](#), [Pinto et al. 2015](#)).

Therefore, turbulent motions alone are below the level required to balance radiative cooling loss (see Fig. 6). This means that dissipation of turbulence by itself may not provide and propagate the amount of energy required to quench cooling (and star formation) in the cool core and gives a natural explanation for the coexistence of the powerful AGN, strong cooling and starburst. AGN feedback and its effects may be insufficient to compete with the massive amount of

³ <https://heasarc.gsfc.nasa.gov/xstar/docs/html/node106.html>

cool gas in the core of the cluster. Alternatively, it is possible that the energy necessary to quench cooling is transported via sound waves as suggested by Fabian et al. (2017) and Bambic et al. (2018). The high star formation itself may be provoked by Compton cooling due to the strong AGN radiation (e.g. McDonald et al. 2015 and Walker et al. 2014). In the outer regions, weak shocks produced by mergers and sloshing, travelling at mildly supersonic velocities, may provide a further source of heating (e.g. Ascasibar & Markevitch 2006, Lau et al. 2009 and Walker et al. submitted).

The abundance pattern that we measure in the Phoenix RGS spectrum is consistent with the estimates obtained with CCD spectra (Tozzi et al. 2015) and broadly agrees with the abundances commonly found in nearby cool core clusters (Mernier et al. 2016). This suggests that there are not significant differences between the Phoenix cluster, a prototype high- z massive cluster, and the nearby cool core clusters.

It is striking to notice that the Phoenix cluster exhibits high cooling and star formation rates if compared to smaller cool cores where the predicted cooling rates are much larger than than the actual measurements of cooling rates and star formation rates. According to McDonald et al. (2018) there is a significant trend in the ratio between the star formation and the cooling rates above $\sim 30 M_{\odot} \text{ yr}^{-1}$. They interpret the trend as an increasing efficiency with which the ICM cools and forms stars in the strongest cool cores such as Abell 1835 ($\sim 140 M_{\odot} \text{ yr}^{-1}$, see Sanders et al. 2010) and Phoenix ($\sim 350 M_{\odot} \text{ yr}^{-1}$, our value). As McDonald et al. (2018) pointed out, large cooling rates may result in high accretion onto the supermassive black holes, which can progressively switch from a kinetic/radio to a quasar/radiative feedback mode. This could somehow lower the efficiency of quenching star formation due to a possible lower energy release by radiation compared to powerful radio jets (see e.g. Churazov et al. 2005) and change the way cooling actually occurs with lower ICM emission of soft X-rays (Compton cooling, see also Walker et al. 2014).

4.3 Future missions: *XRISM* and *ATHENA*

Current X-ray instruments that enable direct velocity measurements such as the gratings on board *XMM-Newton* and *Chandra* and their CCD/imaging detectors that allow us to obtain indirect velocity measurements have several limitations (see, e.g., Sect. 1 and references therein).

The most accurate, direct, measurement of line broadening and, therefore, constraint on turbulence, was obtained by the *Hitomi* satellite during its deep (230ks) observation of the Perseus cluster of galaxies (Hitomi Collaboration 2016). The soft X-ray spectrometer (SXS) microcalorimeter on-board *Hitomi* enabled to measure an average line broadening of $164 \pm 10 \text{ km s}^{-1}$ and possible lower than 100 km s^{-1} once PSF effects were taken into account (Hitomi Collaboration 2017). This started to cast doubts on the efficiency of turbulence to propagate the heat throughout the cluster rapidly enough to offset radiative losses (see also Fabian et al. 2017).

Due to a chain of unfortunate circumstances, *Hitomi* (also known as *ASTRO-H*, Takahashi et al. 2010) was lost, but a new X-Ray Imaging and Spectroscopy Mission

(*XRISM*, a.k.a *XARM*⁴, X-ray Astronomy Recovery Mission) has been accepted and will be likely launched in 2022 (see, e.g., Guainazzi & Tashiro 2019).

Here we perform a simulation of the Phoenix cluster as it will be seen by *XRISM* using the *Hitomi*/SXS 5 eV response matrix (see Fig. 7, bottom panel). We adopt our *XMM-Newton*/RGS best fit model consisting of two thermal models with temperatures of 1.2 and 7.0 keV, see Sect. 3.4 and Table 2 plus photoionized gas that reproduces the Fe XVII X-ray emission and the O VI UV flux as measured by McDonald et al. (2015). We assume 250ks exposure time, similar to the Perseus cluster, but with the gate valve open (GVO). We also take into account the emission from the central AGN by adding the model of Tozzi et al. (2015), which consists of an intrinsically-absorbed ($N_{\text{H}} = 5 \times 10^{23} \text{ cm}^{-2}$) power-law with slope 1.8 and an unabsorbed intrinsic luminosity of $5 \times 10^{45} \text{ erg s}^{-1}$ in the 2-10 keV energy band. We remind the reader that the RGS template model is obtained for a region that can be approximated with a square of 50 arc second side.

We adopt a line broadening of 250 km s^{-1} , which is well within our upper-limits obtained by subtracting the spatial broadening. Despite the much larger distance of the Phoenix ($z = 0.6$) compared to the Perseus cluster ($z = 0.018$), we will obtain a statistical uncertainty of just 25 km s^{-1} (i.e. 10%) for a 250ks *XRISM* observation. This is due to the brightness of the Phoenix cluster and its high temperature, which boosts the Fe K (Fe XXIV-XXVI) emission lines where the *XRISM* resolving power peaks (see Fig. 7, bottom panel). This accuracy is high enough to distinguish between some different heating mechanisms.

The X-ray Integral Field Unit (X-IFU) on board the Advanced Telescope for High Energy Astrophysics (*ATHENA*, Nandra et al. 2013) will provide a drastic improvement in both spatial resolution (from 1 arc minute down to around 5 arc seconds), spectral resolution (from 5 eV to 2.5 eV) and effective area (more than an order of magnitude larger than any previous grating or microcalorimeter). For the astrophysics of galaxy clusters this means an improvement of two orders of magnitude in our capabilities. In Fig. 7, top panel, we show a simulation of the Phoenix cluster made with the same template model used above, but with a short exposure time of just 10ks. Both the foreground emission from our Galaxy, the Local Bubble and non X-ray background due to highly-energetic particles are taken into account following the mission requirements⁵. The sky region is a square of 50 arc second side as above.

The X-IFU 10ks snapshot of the Phoenix cluster will provide a spectacular spectrum of high quality and yield statistical uncertainties of 9 km s^{-1} (i.e. $\sim 4\%$) on the velocity broadening. If we include - in quadrature - additional systematic uncertainties due to gain homogeneity, stacking of nearby pixels within the 50 arc second area and uncertainty in the spectral resolution, we may get an uncertainty of up to $15\text{-}20 \text{ km s}^{-1}$ (i.e. 6 – 8%, which is well above the 5σ level). The current mission requirement for the effective area is 1.4 m^2 at 1 keV. This will not produce any major is-

⁴ <https://heasarc.gsfc.nasa.gov/docs/xarm/>

⁵ <http://www.the-athena-x-ray-observatory.eu/resources/simulation-tools.html>

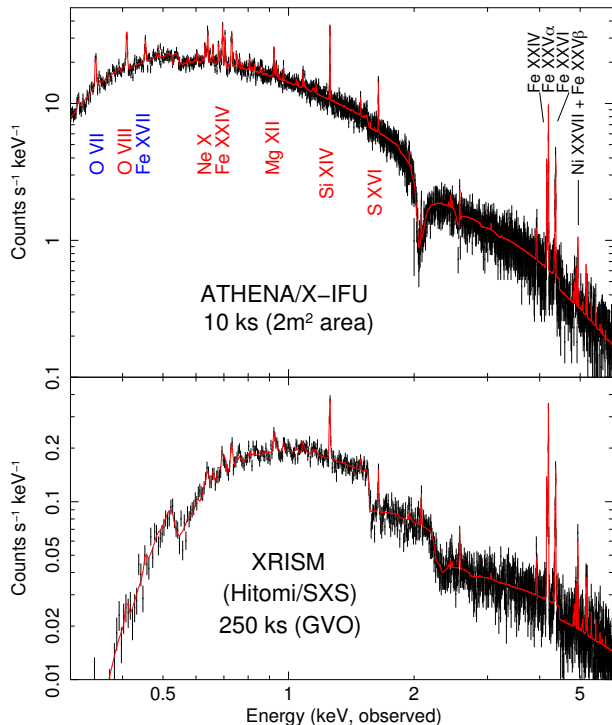


Figure 7. Simulations of the Phoenix cluster for a region of 50 arc second size adopting the XMM-Newton/RGS best fit model plus the AGN and the cool (< 2 keV) gas (see text). Cosmic X-ray background and particle background are accounted for. The strongest transitions are labelled in the observed frame (we adopt $z = 0.596$ and turbulence broadening $v_{1D} = 250$ km s $^{-1}$). We use the response matrix of *Hitomi*/SXS as a proxy for *XRISM*.

sues for these measurements because the accuracy is driven by the high-energy band above 2 keV apart from a small increase of the exposure time. Moreover, the 5 arc second spatial resolution of the X-IFU will enable us to perform accurate measurements of turbulent velocities in more than 20 different regions of the cool core for an exposure time of just 100 ks.

The Phoenix cluster is an extraordinary, bright, cooling core cluster producing X-ray spectra with strong emission lines. However, the X-IFU will enable accurate turbulence measurements with 10 – 20% uncertainties (i.e. 5σ) for several clusters at high redshift - at high AGN feedback and star formation rates - and fairly short (50-100 ks) exposures.

5 CONCLUSIONS

The Phoenix cluster (SPT-CLJ2344-4243) is the most luminous X-ray cluster known and the most distant cluster observed with high-resolution X-ray spectrometers. It exhibits an outstanding starburst of $500 - 800 M_{\odot} \text{ yr}^{-1}$, which is among the largest found in the local Universe ($z < 1$), and an AGN inflating bubbles via powerful radio jets. The presence of high star formation and cooling rates in combination with a powerful AGN is puzzling if compared to the low rates shown by nearby cooling core clusters. In this work, we perform an in-depth study of the XMM-Newton observations of the Phoenix cluster with particular focus on the

high-resolution spectrometers in order to obtain accurate measurements of the cooling rate and turbulent broadening.

We find that about $220 - 480 M_{\odot} \text{ yr}^{-1}$ are cooling below 2 keV in the cluster core, in broad agreement with the estimates of star formation rate, and that the turbulence level is likely not adequate to fully propagate AGN heating throughout the cool core. This provides a natural explanation for the coexistence of a large amounts of cool gas, star formation and a powerful AGN in the Phoenix cluster. However, the comparison with nearby, more quiescent, cool core clusters suggests that the discrepancy is likely due to either to the younger age of the Phoenix cluster, and therefore of the BCG AGN feedback activity, or the accretion rate on the supermassive black hole and the feedback mode.

Future missions such as *ATHENA* and *XRISM* will boost the accuracy in measuring crucial parameters in X-ray spectra of clusters of galaxies. In particular, we show that for Phoenix-like clusters it is possible to obtain excellent results - such as a 5σ detection of turbulence - with short snapshots of about 10ks exposure.

ACKNOWLEDGMENTS

This work is based on observations obtained with XMM-Newton, an ESA science mission funded by ESA Member States and USA (NASA). We acknowledge support from ERC Advanced Grant Feedback 340442. We also thank J. de Plaa and J. Kaastra for support in optimising SPEX. We also acknowledge the anonymous referee for useful comments that have improved the clarity of the manuscript.

REFERENCES

- Ascasibar Y., Markevitch M., 2006, ApJ, 650, 102
- Bambic C. J., Pinto C., Fabian A. C., Sanders J. S., Reynolds C. S., 2018, ArXiv e-prints
- Bregman J. N., Fabian A. C., Miller E. D., Irwin J. A., 2006, ApJ, 642, 746
- Bregman J. N., Miller E. D., Athey A. E., Irwin J. A., 2005, ApJ, 635, 1031
- Churazov E., Forman W., Jones C., Böhringer H., 2000, A&A, 356, 788
- Churazov E., Sazonov S., Sunyaev R., Forman W., Jones C., Böhringer H., 2005, MNRAS, 363, L91
- de Plaa J., Zhuravleva I., Werner N., Kaastra J. S., Churazov E. e. a., 2012, A&A, 539, A34
- den Herder J. W., Brinkman A. C., Kahn S. M., Branduardi-Raymont G., Thomsen K. e. a., 2001, A&A, 365, L7
- Eckert D., Gaspari M., Vazza F., Gastaldello F., Tramacere A., Zimmer S., Ettori S., Paltani S., 2017, ApJL, 843, L29
- Fabian A. C., 1994, ARA&A, 32, 277
- Fabian A. C., 2012, ARA&A, 50, 455
- Fabian A. C., Sanders J. S., Allen S. W., Crawford C. S., Iwasawa K., Johnstone R. M., Schmidt R. W., Taylor G. B., 2003, MNRAS, 344, L43
- Fabian A. C., Walker S. A., Russell H. R., Pinto C., Sanders J. S., Reynolds C. S., 2017, MNRAS, 464, L1

- Guainazzi M., Tashiro M. S., 2019, Proceedings of the IAU Symposium No. IAUS342, “Perseus in Sicily: from black hole to cluster outskirts”
- Hitomi Collaboration 2016, *Nature*, 535, 117
- Hitomi Collaboration 2017, ArXiv e-prints
- Hlavacek-Larrondo J., Fabian A. C., Edge A. C., Ebeling H., Sanders J. S., Hogan M. T., Taylor G. B., 2012, *MNRAS*, 421, 1360
- Hudson D. S., Mittal R., Reiprich T. H., Nulsen P. E. J., Andernach H., Sarazin C. L., 2010, *ApJ*, 513, A37
- Kalberla P. M. W., Burton W. B., Hartmann D., Arnal E. M., Bajaja E., Morras R., Pöppel W. G. L., 2005, *A&A*, 440, 775
- Lau E. T., Kravtsov A. V., Nagai D., 2009, *ApJ*, 705, 1129
- Lodders K., Palme H., 2009, *Meteoritics and Planetary Science Supplement*, 72, 5154
- McDonald M., Bayliss M., Benson B. A., Foley R. J., Ruel J. e. a., 2012, *Nature*, 488, 349
- McDonald M., Benson B. A., Vikhlinin A., Stalder B., Bleem L. E. e. a., 2013, *ApJ*, 774, 23
- McDonald M., Gaspari M., McNamara B. R., Tremblay G. R., 2018, ArXiv e-prints
- McDonald M., McNamara B. R., van Weeren R. J., Applegate D. E., Bayliss M. e. a., 2015, *ApJ*, 811, 111
- McNamara B. R., Nulsen P. E. J., 2007, *ARA&A*, 45, 117
- McNamara B. R., Russell H. R., Nulsen P. E. J., Edge A. C., Murray N. W. e. a., 2014, *ApJ*, 785, 44
- Mernier F., de Plaa J., Pinto C., Kaastra J. S., Kosec P., Zhang Y.-Y., Mao J., Werner N., 2016, *A&A*, 592, A157
- Mittal R., McDonald M., Whelan J. T., Bruzual G., 2017, *MNRAS*, 465, 3143
- Nandra K., Barret D., Barcons X., Fabian A., den Herder J.-W., Piro L., Watson M., Adami C., Aird J., Afonso J. M., et al. 2013, ArXiv e-prints
- Ogorzalek A., Zhuravleva I., Allen S. W., Pinto C., Werner N., Mantz A. B., Canning R. E. A., Fabian A. C., Kaastra J. S., de Plaa J., 2017, *MNRAS*, 472, 1659
- Peterson J. R., Kahn S. M., Paerels F. B. S., Kaastra J. S., Tamura T., Bleeker J. A. M., Ferrigno C., Jernigan J. G., 2003, *A&A*, 590, 207
- Pinto C., Fabian A. C., Ogorzalek A., Zhuravleva I., Werner N., Sanders J., Zhang Y.-Y., Gu L., de Plaa J., Ahoranta J., Finoguenov A., Johnstone R., Canning R. E. A., 2016, *MNRAS*, 461, 2077
- Pinto C., Fabian A. C., Werner N., Kosec P., Ahoranta J., de Plaa J., Kaastra J. S., Sanders J. S., Zhang Y.-Y., Finoguenov A., 2014, *A&A*, 572, L8
- Pinto C., Kaastra J. S., Costantini E., de Vries C., 2013, *A&A*, 551, A25
- Pinto C., Middleton M. J., Fabian A. C., 2016, *Nature*, 533, 64
- Pinto C., Sanders J. S., Werner N., de Plaa J., Fabian A. C., Zhang Y.-Y., Kaastra J. S., Finoguenov A., Ahoranta J., 2015, *A&A*, 575, A38
- Russell H. R., McDonald M., McNamara B. R., Fabian A. C., Nulsen P. E. J. e. a., 2017, *ApJ*, 836, 130
- Russell H. R., McNamara B. R., Edge A. C., Nulsen P. E. J., Main R. A. e. a., 2014, *ApJ*, 784, 78
- Sanders J. S., Fabian A. C., 2011, *MNRAS*, 412, L35
- Sanders J. S., Fabian A. C., 2012, *MNRAS*, 421, 726
- Sanders J. S., Fabian A. C., 2013, *MNRAS*, 429, 2727
- Sanders J. S., Fabian A. C., Russell H. R., Walker S. A., 2018, *MNRAS*, 474, 1065
- Sanders J. S., Fabian A. C., Smith R. K., Peterson J. R., 2010, *MNRAS*, 402, L11
- Takahashi T., Mitsuda K., Kelley R., Aharonian F., Akimoto F. e. a., 2010, in *Soc. of Photo-Optical Inst. Eng. Conf. Ser. Vol. 7732 of Soc. of Photo-Optical Inst. Eng. Conf. Ser.*, The ASTRO-H Mission
- Tozzi P., Gastaldello F., Molendi S., Ettori S., Santos J. S., De Grandi S., Balestra I., Rosati P., Altieri B., Cresci G., Menanteau F., Valtchanov I., 2015, *A&A*, 580, A6
- Walker S. A., Fabian A. C., Russell H. R., Sanders J. S., 2014, *MNRAS*, 442, 2809
- Walker S. A., Sanders J. S., Fabian A. C., 2015, *MNRAS*, 453, 3699
- Werner N., Zhuravleva I., Churazov E., Simionescu A., Allen S. W., Forman W., Jones C., Kaastra J. S., 2009, *MNRAS*, 398, 23
- Williamson R., Benson B. A., High F. W., Vanderlinde K., Ade P. A. R. e. a., 2011, *ApJ*, 738, 139
- Zhuravleva I., Churazov E., Schekochihin A. A., Allen S. W., Arévalo P. e. a., 2014, *Nature*, 515, 85

This paper has been typeset from a $\text{\TeX}/\text{\LaTeX}$ file prepared by the author.

APPENDIX A: RGS BACKGROUND

In this section we briefly compare the raw source spectrum of the Phoenix cluster and two background spectra computed with different methods. As mentioned in Section 2.1, the RGS 1 and 2 spectra are extracted using as centroid $(\alpha, \delta) = (23 : 44 : 43.9, -42 : 43 : 13.7)$ for all observations and a width of 50 arcsec ($xpsfincl = 90$ in the *rgsproc*). In order to subtract the background we test both the standard background spectrum which is extracted beyond the 98% of the RGS point spread function (PSF, $xpsfexcl = 98$ in the *rgsproc*) and the model background spectrum, which is a template background spectrum computed using blank field observations and normalized by the count rate in CCD9. Both are computed by the *rgsproc* task. Extended, nearby ($z < 0.2$), clusters would contaminate the background extraction region ($< 2'$) with source photons. However, the Phoenix cluster has a high distance ($z = 0.6$) and the background spectrum extracted beyond the 98% of the PSF is rather clean and is comparable to the model background spectrum. For display purposes we stack the source raw spectra, the observation and model background spectra and show them in Fig. A1. We notice that the background spectra are similar and, therefore, the choice of using the one or the other does not affect the results. The source is brighter than the background up to about 30 Å, where the O VIII line clearly exceeds it.

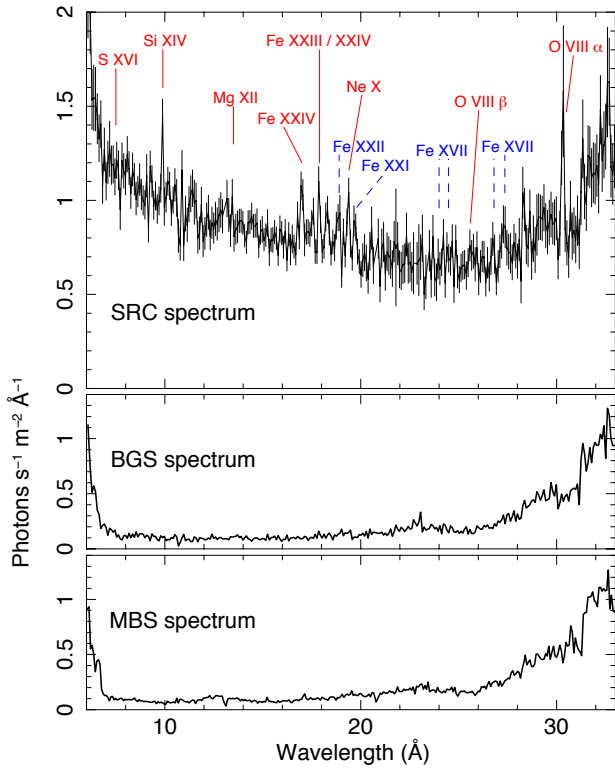


Figure A1. XMM-Newton/RGS raw spectra for the source (top panel, without any background subtraction), the background as determined from the exposure outside the 98% of the PSF (BGS, middle panel) and the model background computed from templates from blank field observations (MBS, bottom panel).